

Simulation on plasma discharge and transport in large and complex geometric space

Shiyi Tang(汤诗奕), Mengran Xiao(肖梦然), Ziqi Ma(马梓淇), Dongjie Yang(杨东杰), Xiaokai An(安小凯), Liangliang Liu(刘亮亮), Suihan Cui(崔岁寒), Ricky K. Y. Fu(傅劲裕), Paul K. Chu(朱剑豪), and Zhongzhen Wu(吴忠振)

Citation: Chin. Phys. B, 2026, 35 (**3**): 035202. DOI: 10.1088/1674-1056/adfebe
http://cpb.iphy.ac.cn; http://iopscience.iop.org/cpb

What follows is a list of articles you may be interested in

Optimization of an *m* = 0 multi-loop helicon source configuration for linear plasma devices: A comparative study with Boswell and half-helix antenna designs

Yi Yu(余羿), Hao Liu(刘灏), Xue-Dong Huang(黄学栋), Chen-Yu Xiao(肖晨雨), Lin Nie(聂林), Guang-Yi Zhao(赵光义), and Min Xu(许敏)

Chin. Phys. B, 2025, 34 (**12**): 125202. DOI: 10.1088/1674-1056/ade24b

New progress on DC H_2^+ beam generation: Tens of mA output and 70% fraction from a 2.45 GHz microwave driven ion source

Bujian Cui(崔步坚), Shixiang Peng(彭士香), Jianbin Zhu(朱建斌), Yicheng Dong(董宜承), Zhiyu Guo(郭之虞), and Jiaer Chen(陈佳洱)

Chin. Phys. B, 2025, 34 (**8**): 085203. DOI: 10.1088/1674-1056/adf1ec

Power transfer efficiency in an air-breathing radio frequency ion thruster

Gao-Huang Huang(黄高煌), Hong Li(李宏), Fei Gao(高飞), and You-Nian Wang(王友年)

Chin. Phys. B, 2024, 33 (**7**): 075201. DOI: 10.1088/1674-1056/ad426c

Transition from a filamentary mode to a diffuse one with varying distance from needle to stream of an argon plasma jet

Hui-Min Xu(许慧敏), Jing-Ge Gao(高敬格), Peng-Ying Jia(贾鹏英), Jun-Xia Ran(冉俊霞), Jun-Yu Chen(陈俊宇), and Jin-Mao Li(李金懋)

Chin. Phys. B, 2024, 33 (**1**): 015205. DOI: 10.1088/1674-1056/ad0149

Efficient hydrophilicity improvement of titanium surface by plasma jet in micro-hollow cathode discharge geometry

Peng-Ying Jia(贾鹏英), Han-Xiao Jia(贾焓潇), Jun-Xia Ran(冉俊霞), Kai-Yue Wu(吴凯玥), Jia-Cun Wu(武珈存), Xue-Xia Pang(庞学霞), and Xue-Chen Li(李雪辰)

Chin. Phys. B, 2023, 32 (**8**): 085202. DOI: 10.1088/1674-1056/acbde9

Simulation on plasma discharge and transport in large and complex geometric space

Shiyi Tang(汤诗奕)[1,†], Mengran Xiao(肖梦然)[1,†], Ziqi Ma(马梓淇)[1], Dongjie Yang(杨东杰)[1], Xiaokai An(安小凯)[1], Liangliang Liu(刘亮亮)[1,2], Suihan Cui(崔岁寒)[1,2,‡], Ricky K. Y. Fu(傅劲裕)[2], Paul K. Chu(朱剑豪)[2], and Zhongzhen Wu(吴忠振)[1,§]

[1] *School of Advanced Materials, Peking University Shenzhen Graduate School, Shenzhen* 518055, *China*

[2] *Department of Physics, Department of Materials Science and Engineering, and Department of Biomedical Engineering, City University of Hong Kong, Tat Chee Avenue, Kowloon, Hong Kong, China*

(Received 7 May 2025; revised manuscript received 19 August 2025; accepted manuscript online 25 August 2025)

The plasma discharge and transport properties in the vacuum systems is critical for film deposition controlling. However, industrial-scale vacuum systems usually exhibit large and complex geometries, leading to boundary distortion and convergence difficulty in the conventional simulation techniques. In this work, a PIC/MCC model with FEM solver for non-uniform grids is established to precisely construct a large simulation domain with complex boundaries using the fluid model, and tracks the charged particle movements in non-uniform electromagnetic fields by the PIC/MCC method. The discharge process in a large cylindrical vacuum chamber shows the obvious interaction between the spatial electromagnetic field and plasma. The distribution of deposited ions is consistent with the potential gradient of the sheath. Besides, the ion deposition proportion is increased by more than 3 times and the average ion energy is increased by over 45.0 eV compared with the constant potential, indicating that the background electric field plays a significant role. When the spatial potential is steady, the plasma leads to stable accumulation with the peak density of 10^{15} m^{-3} achieving convergence at 0.3 μs, thus demonstrating the excellent operation speed and convergence compared to the individual fluid model and PIC/MCC method. The density of the computational grids modified further according to the Debye length reveals a significantly improved computational performance with the convergence process compressed into 0.26 μs and the total runtime reduced by 40%.

Keywords: large and complex geometric space, PIC/MCC model with FEM solver for non-uniform grids, discharge and transport properties, computation performance

PACS: 52.50.Dg, 52.55.Jd, 52.65.Rr, 52.65.Pp

DOI: 10.1088/1674-1056/adfebe **CSTR:** 32038.14.CPB.adfebe

1. Introduction

Magnetron sputtering technology is widely used in the industrial production of functional coatings. Currently, the requirements for higher coating quality and performance grow, and there is an increasing need to achieve large-scale, mass production capabilities. To address industrial demand, vacuum systems require more diversified configurations such as multi-target co-sputtering, multi-source coupling, auxiliary anode, and substrate bias, which significantly exacerbate the influence of the spatial fields on the plasma. Consequently, the plasma presents a wider distribution and more complex behavior,[1] thus increasing the difficulty in detection and control.[2] Therefore, predicting the plasma discharge and transport properties in the large-scale vacuum chamber by simulation is important.

Among the existing plasma simulation techniques,[3] the interactions between the spatial electromagnetic field and plasma are usually determined by the fluid model[4–6] and particle-in-cell/Monte Carlo collision (PIC/MCC) method.[7–9] Generally, establishing equations for physical processes is suitable for simulating vacuum systems with a large size and complex geometry.[10] For example, the fluid model derives the plasma discharge and transport in the vacuum chamber by solving a set of partial differential equations composed of the continuity equation, momentum conservation equation, Poisson equation, and electron Boltzmann relation.[11] However, the continuity equation assumes that the magnetic field strength is small and constant, but it can distort the results in actual vacuum systems with extremely inhomogeneous distribution of the field.[12] Contin *et al.*[11] have used magnetohydrodynamic equations coupled with the continuity equation to describe the inhomogeneous fields, but the partial differential equations are generally unsolvable and show poor convergence. Jimenez *et al.*[13,14] have used the particle Monte Carlo (MC) method[15] to solve the reaction and transport rates of plasmas in inhomogeneous fields and substituted them into the continuity equation to simplify the calculation. However, the model must use the test particle MC module repeatedly,

[†]These authors contributed equally to this work.

[‡]Corresponding author. E-mail: cuish@pku.edu.cn

[§]Corresponding author. E-mail: wuzz@pku.edu.cn

© 2026 Chinese Physical Society and IOP Publishing Ltd. All rights, including for text and data mining, AI training, and similar technologies, are reserved.

resulting in a slower calculation speed and poor convergence. Compared with the fluid model, the PIC/MCC method simplifies the calculation process of partial differential equations into the solution of the Poisson's equation by directly tracking the movements and collisions of charged particles in the electromagnetic field to improve the convergence.[16] However, the PIC/MCC method, which is typically based on rectangular grids with a uniform density and suffers a large calculation amount, is only suitable for small regular areas with dimensions less than 200 mm×200 mm.[17] For a large geometrically complex space, Vay *et al.*[18,19] have developed the multigrid method to improve the computational speed, which is, to approximate the solution on coarse grids first and then refine it step by step to obtain an accurate solution. However, the iteration calculation process from large grid to small grid step by step always decreases the convergence.[2,20] Banegas *et al.*[21] have developed the fast Fourier transform method to replace the finite difference method and improve the computational efficiency, but the Fourier transform is still only suitable for regular areas.[22] Consequently, it is evident that neither the fluid model nor the PIC/MCC method can independently simulate the plasma discharge and transport behavior in large vacuum chambers, but their advantages and disadvantages are quite clear respectively.

In this work, a large simulation domain with complex boundaries is constructed and non-uniform triangular grids are set using the fluid model first, and then the plasma discharge and transport in the inhomogeneous field are tracked by the PIC/MCC method, resulting in the PIC/MCC model with fluid-based electric field solver (denote as PIC/MCC model with FEM solver for non-uniform grids). By using this model, the discharge process of a planar cathode in a large cylindrical vacuum chamber is simulated, and the results reveal obvious interactions between the spatial electromagnetic field and plasma on the vacuum chamber scale. The anode sheaths generate near the internal and external anode boundaries, which in turn influence the ion deposition process. The model achieves convergence at 0.3 μs, with the potential reaching a steady state and the plasma forming stable accumulation. By adjusting the computational grids according to the Debye length, the convergence process is further shortened to 0.26 μs, and the total running time is reduced by 40%.

2. Methods

The models were independently developed with the MATLAB R2022b software. To ensure computational efficiency, the calculations were performed on a high-performance computing cluster (Intel (R) Xeon (R) CPU E5-2650 v3 @ 2.30 GHz).

2.1. Simulation domain

The simulation domain with complex boundaries is constructed using the MATLAB PDETOOL toolbox. The simulation object is the discharge of a planar cathode in a large cylindrical vacuum chamber. The cross-section along the height direction of the cylindrical vacuum chamber is the simulation domain in our model. Therefore, the simulation domain is a two-dimensional circular region, as shown in Fig. 1(a). Because the cathode is located on the sidewall of the chamber, the red dashed line is a diameter of the circle which pass through the center point of the cross-sectional cathode, which is also the symmetry axis of the simulation domain. The circular area $\boldsymbol{Z}_1$ represents the vacuum chamber with a diameter of 600 mm, and $\boldsymbol{Z}_2$ represents the magnetron cathode, including the target (green area), the cathode-anode gap (purple area), and the anode (dark blue area) with widths of 120 mm, 1.5 mm, and 7.3 mm, respectively. $\boldsymbol{Z}_3$ represents the substrate with a size of 120 mm×0.5 mm, and the target-substrate distance is 150 mm. Owing to the geometric symmetry, the simulation domain is simplified to half (right half of Fig. 1(a)). The background magnetic field is provided by the cathode (left half of Fig. 1(a)), and the influence of the plasma on the magnetic field is ignored during the simulation.[23] The discharge pressure is 1.0 Pa, and the working gas is Ar. The target potential is set to −500 V, and the anode, vacuum chamber walls, and substrate are all grounded. The simulation domain includes four types of boundaries, namely cathode condition (green), anode boundary (blue), transitional boundary (purple), and symmetrical boundary (red), as shown in Fig. 1(b). The cathode boundary represents the target surface with a potential $\varphi = -500$ V. The anode boundary includes the anode, vacuum chamber wall, and substrate with a potential $\varphi = 0$ V. The transitional boundary lies between the target and anode, expressed by $\varphi = 1000x/3 - 20500$ V assuming a linear variation in this interval 60 mm$\leq x \leq$61.5 mm (The voltage is −500 V and 0 V at 60 mm and 61.5 mm, respectively). The symmetrical boundary represents the axis of symmetry of the simulation domain, so that the normal potential gradient in the normal direction is equal to 0, that is $\partial\varphi/\partial x = 0$.

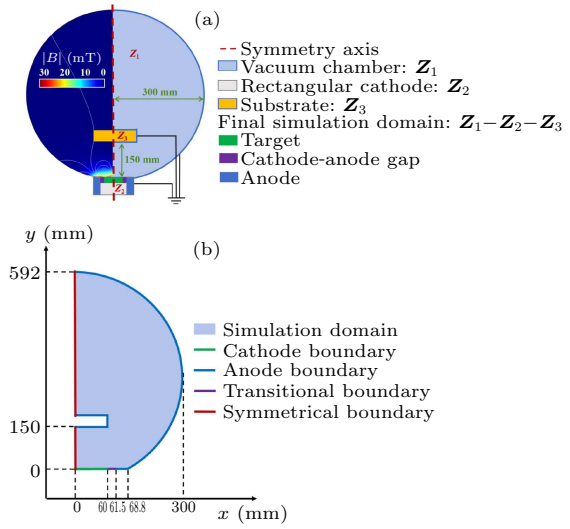


Fig. 1. Schematic diagrams: (a) model simulation domain and (b) boundary conditions.

2.2. Non-uniform grid division

Figures 2(a)–2(c) show the initial distributions of the electric and magnetic fields in the simulation domain, revealing that the background fields have inhomogeneous distributions. To ensure the computational speed and accuracy, the fluid model is used to construct non-uniform grids matching the distributions of the fields.[12] Figures 2(d)–2(f) show the enlarged view of the area in which the electric and magnetic fields have higher intensities and larger gradients (area surrounded by the black lines in Figs. 2(a)–2(c), defined as the grid refinement area $\boldsymbol{Q}$). In the space of 0 mm$\leq y \leq$60 mm, the electric and magnetic fields vary in the range of 3×10^3 V/m–1×10^4 V/m and 1 mT–30 mT, respectively, showing large variations and significant distribution differences. Hence, this area is defined as the strong background gradient area (the gray area in Fig. 2(f)) and divided with ultra-fine grids of 1×10^{-4} m. In comparison, the intensities of the electric and magnetic fields in the space of 60 mm$\leq y \leq$150 mm decrease to below 3000 V/m and 1 mT, respectively, and the variation range narrows significantly. This area is defined as the weak background gradient area (the white area in Fig. 2(f)) and divided with relatively fine grids of 5×10^{-4} m. In contrast, the electric and magnetic fields show a smaller intensity and variation gradient in the area outside $\boldsymbol{Q}$, where the effects of the electromagnetic fields on the plasma can only be revealed over a longer range.[24] Therefore, the coarser grids of 1×10^{-2} m are used to divide this area. The actual grid is shown in Fig. A1 of Appendix A.

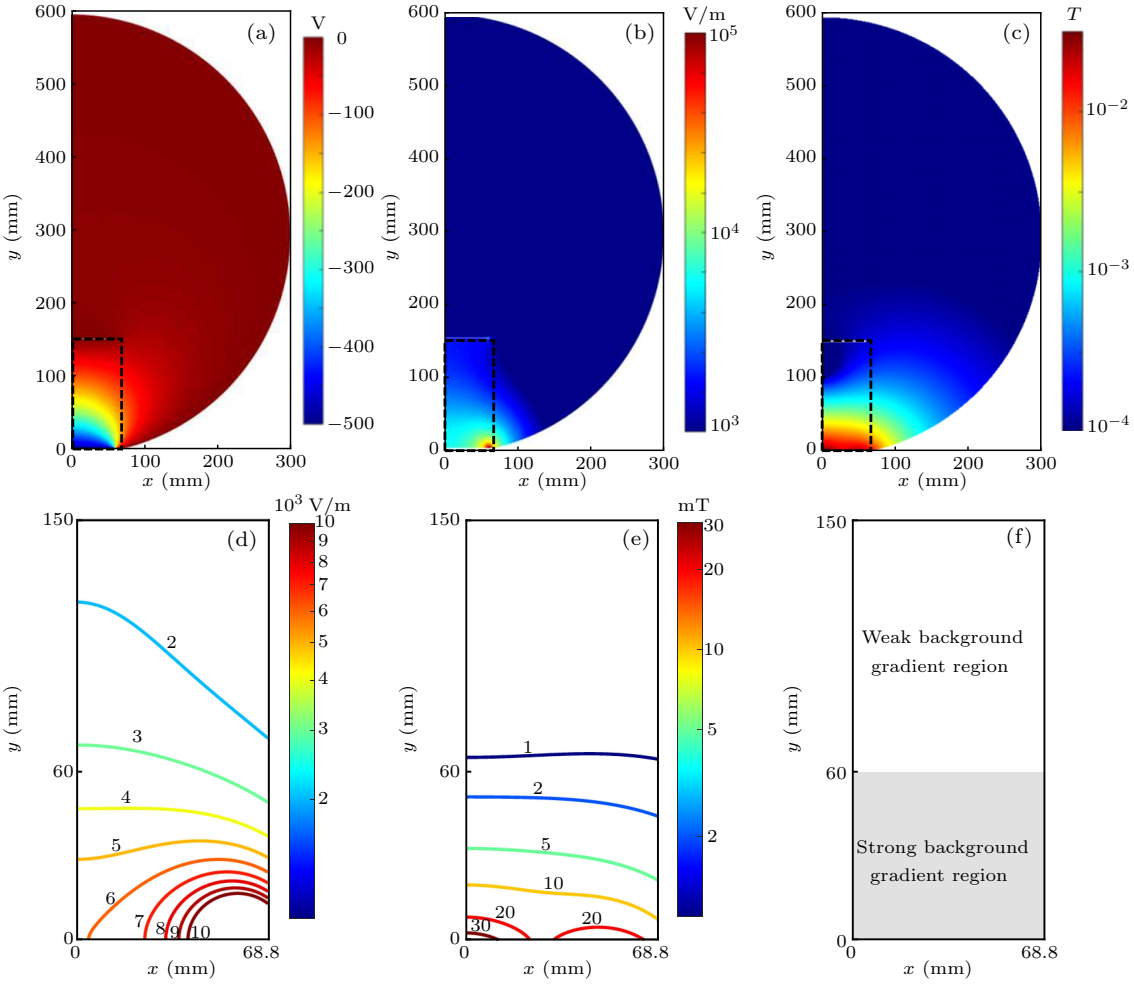


Fig. 2. Initial distributions of (a) potential, (b) electric field, and (c) magnetic induction intensity in the simulation domain; (d) electric field intensity, (e) magnetic induction intensity in the grid refinement area $\boldsymbol{Q}$; (f) schematic diagram of the grid division.

2.3. Plasma discharge and transport simulation

The initial plasma density[23] is set to 1×10^{13} m^{-3}. The macroparticles, including ions and electrons, are uniformly generated in the space of 0 mm $\leq x \leq$60 mm and 0 mm $\leq y \leq$60 mm above the cathode. Each macroparticle represents 1×10^6 actual particles. The initial average temperature of electrons and Ar^+ ions are equal to the background temperature of 300 K, and the velocity of electrons and Ar^+ follows the Maxwell distribution.[23] During the simulation, the electron time step is set to 1×10^{-12} s. Compared with electrons, the specific charge of Ar^+ ions is smaller, so that the ion time step is set to 1×10^{-11} s, which is ten times of the electron time step.[25] The background electric field is updated each ion time step. During the movement, electrons and Ar^+ ions collide continuously and react with the background Ar gas, as shown in Table 1. The macroparticles disappear di-

rectly at the anode or transition boundaries, and rebound at the symmetrical boundary. At the cathode boundary, electrons disappear, while ions sputter the target and release secondary electrons.[26] For convenience, the sputtered target atoms and their subsequent collisions are not considered in this work. According to Clapeyron equation, the density of the background gas N (in unit m^{-3}) can be calculated by

$$N_0 = \frac{pN_\mathrm{A}}{RT}, \tag{1}$$

where $R = 8.314$ J/(mol·K) is the molar gas constant and $N_\mathrm{A} = 6.02 \times 10^{23}$ 1/mol is Avogadro constant. T (in unit K) represents background temperature and p (in unit Pa) represents pressure. Since the Ar^+ ion density ($\sim 10^{15}$ m^{-3}) is much lower than the background Ar atom density ($\sim 10^{20}$ m^{-3}) upon model convergence, the variations in Ar atoms caused by Ar gas ionization is neglected. Therefore, the background Ar atom density is assumed to be constant in the simulation. And particle collision details by MCC method could be found in Appendix A.

Table 1. Main reactions in the Ar gas discharge.[25–27]

Number	Reaction equation	Rate coefficient k ($\mathrm{m}^3\cdot\mathrm{s}^{-1}$)	Threshold (eV)
1	$e + Ar \rightarrow Ar + e$	$2.336\times10^{-14}T_e^{1.609}\times\exp\left(0.0618\,(\ln T_e)^2 - 0.1171\,(\ln T_e)^3\right)$	–
2	$e + Ar \rightarrow Ar^+ + 2e$	$2.34\times10^{-14}T_e^{0.59}\times\exp(-17.44/T_e)$	15.76
3	$e + Ar \rightarrow Ar^m + e$	$2.5\times10^{-15}T_e^{0.74}\times\exp(-11.56/T_e)$	11.56
4	$e + Ar^m \rightarrow Ar^+ + 2e$	$6.8\times10^{-15}T_e^{0.67}\times\exp(-4.2/T_e)$	4.2
5	$e + Ar^m \rightarrow Ar + e$	$4.3\times10^{-16}T_e^{0.74}$	–11.56
6	$Ar^+ + Ar \rightarrow Ar^+ + Ar$	hard-sphere collision	–
7	$Ar^+ + Ar \rightarrow Ar + Ar^+$	hard-sphere collision	–

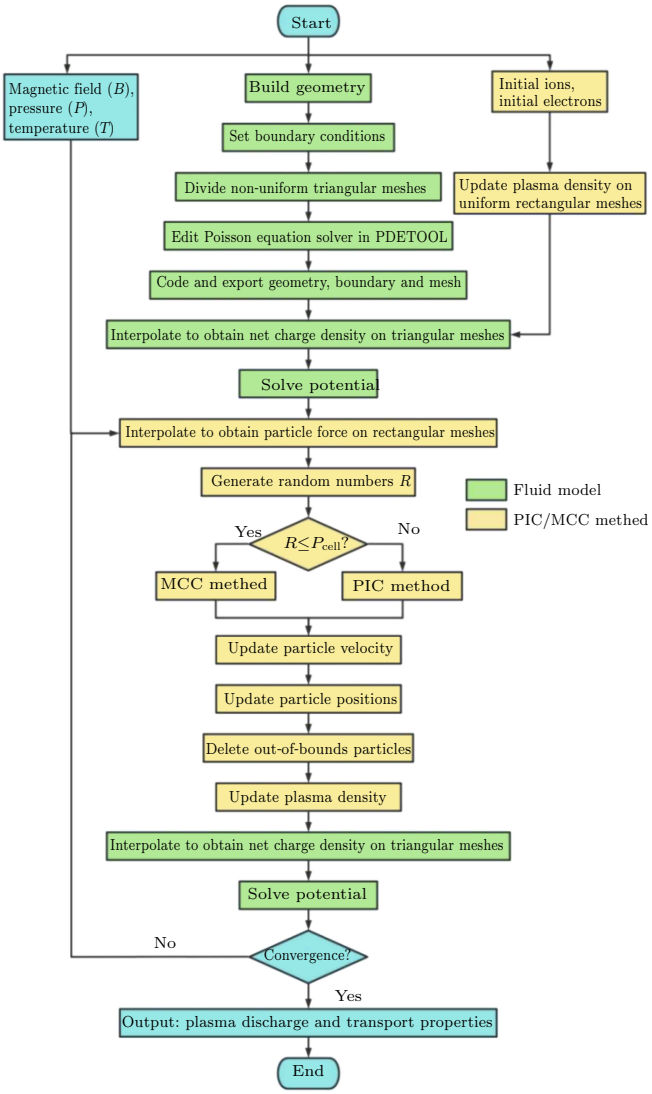


Fig. 3. Workflow of the PIC/MCC model with FEM solver for non-uniform grids.

The workflow of the PIC/MCC model with FEM solver for non-uniform grids is shown in Fig. 3, in which the processes in the green and yellow boxes are operated by the fluid model and PIC/MCC method, respectively. The simulation domain geometry and particle information are generated by the fluid model and PIC/MCC method, respectively, and the loop runs on this basis. In particular, the PIC/MCC method is employed to calculate the plasma density according to the potential on ultra-fine rectangular grids of 1×10^{-4} m (Fig. 2(f)) and then transferred to the non-uniform grids through interpolation, while the fluid model is used to solve the potential according to the plasma density on irregular triangular grids, resulting in an iterative calculation. Parameters (plasma density and potential) transfer between regular and irregular grids is achieved by interpolation and two models (fluid model and PIC/MCC method) are coupled through PDETOOL. The details of PDETOOL could be found in Appendix A. In order to simultaneously improve the operational efficiency and computational stability, the PDETOOL solver with geometry, boundary, and mesh information is transformed into codes before entering the loop, thus enabling the fluid model to directly read the plasma density distribution and assign the output background potential to each charged particle. The particle positions $\boldsymbol{r}$ (in unit m) and velocities $\boldsymbol{v}$ (in unit m/s) are updated based on

$$\begin{cases} \boldsymbol{F} = q_\mathrm{p}(\boldsymbol{E} + \boldsymbol{v}\times\boldsymbol{B}), \\ \boldsymbol{F} = m_\mathrm{p}\dfrac{\mathrm{d}\boldsymbol{v}}{\mathrm{d}t}, \\ \boldsymbol{v} = \dfrac{\mathrm{d}\boldsymbol{r}}{\mathrm{d}t}, \end{cases} \tag{2}$$

where $\boldsymbol{F}$ (in unit N) represents particle force, $\boldsymbol{E}$ (in unit V/m) and $\boldsymbol{B}$ (in unit T) represent the electric field strength and magnetic field strength, respectively, and m_p (in unit kg) and q_p (in

unit C) donate the mass and the charge quantity of the charged particles, respectively. The simulation is considered to reach a steady state when the spatial potential distribution is stable.[7]

3. Results and discussion

Figure 4 displays the computational results of the PIC/MCC model with FEM solver for non-uniform grids in the steady state. The electrons and ions basically show the same density distributions with peak densities over 1.2×10^{15} m^{-3}, indicating that the plasma state is formed.[26] The plasma density distribution in the vacuum chamber is quite inhomogeneous, showing a distribution trend in the density and variation in the gradient generally coinciding with the background fields. In the strong gradient area (gray area in Fig. 2(f)), the electromagnetic field shows the strongest constraint effects on the plasma, resulting in an intense discharge and stable plasma accumulation. In comparison, the constraint effect is significantly reduced in the weak gradient area (white area in Fig. 2(f)), but it still plays a guiding role in the plasma transport,[24] which leads to the difference in the plasma density gradient in different directions.

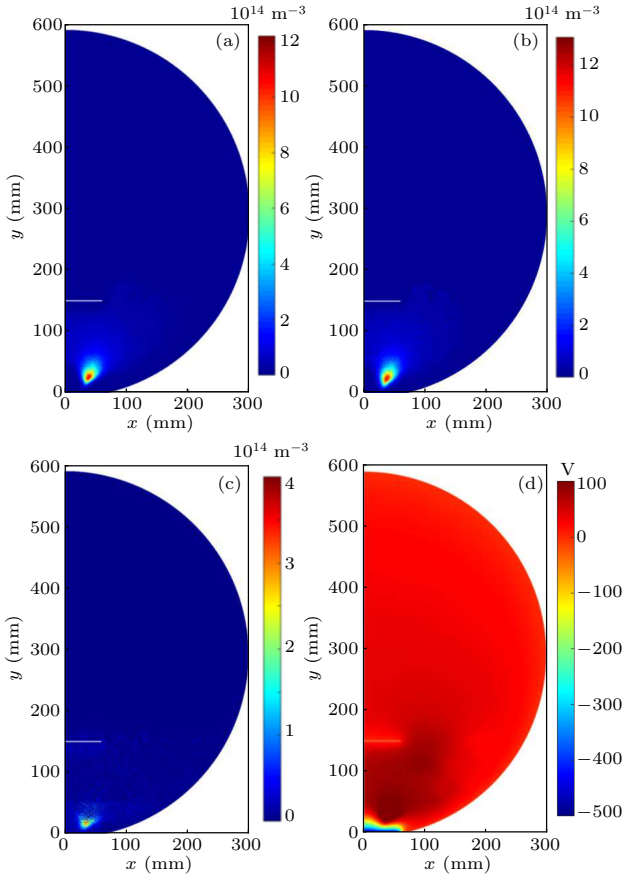


Fig. 4. Steady-state distributions: (a) electron density, (b) ion density, (c) net charge density, and (d) spatial potential calculated by the PIC/MCC model with FEM solver for non-uniform grids.

According to the Poisson equation (Eq. (3)), the plasma discharge and transport processes cause the variation of the spatial net charge density ρ (in unit C/m^3), which in turn affects the spatial potential φ (in unit V):

$$\nabla^2\varphi = -\rho/\varepsilon_0, \tag{3}$$

where $\varepsilon_0 = 8.85\times10^{-12}$ F/m is the vacuum permittivity. Since the initial net charge density in the simulation domain is zero, the potential between the cathode (−500 V) and anode (0 V) exhibits a uniform linear variation, as shown in Fig. 2(a). When the discharge reaches a steady state, the plasma accumulates in the discharge area and forms a sheath above the cathode. At this time, the spatial net charge shows an inhomogeneous distribution, and the spatial potential loses the linear variation characteristics, as shown in Figs. 4(c) and 4(d). In the sheath, the ion density is higher than the electron density, resulting in a high net charge density and large potential gradient.[26] Differently, the plasma outside the sheath is electrically neutral, so that the net charge density is almost zero,[26] thereby showing a gentle potential variation. Except for the sheath region, the electric potential in the whole simulation domain is over 0 V, indicating that the influence of plasma spatial distribution on the electric field permeates the entire vacuum chamber.

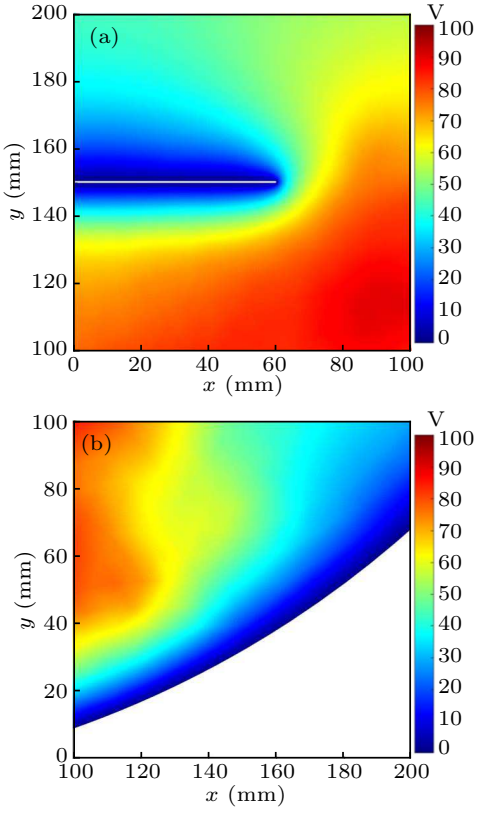


Fig. 5. Distributions of the anode sheath: (a) substrate surface and (b) vacuum chamber wall surface.

As the anode boundary, the potential of the substrate and vacuum chamber wall is set to 0 V. Figure 5(a) displays the potential distribution near the substrate, revealing that a potential difference on both sides of the substrate. In particular, the equipotential lines near the substrate surface facing the target are essentially parallel, indicating that the potential gradient

is nearly constant. This is attributed to the uniform plasma density distribution, yielding almost the same effect on raising the spatial potential. In comparison, the equipotential lines on the other side of the substrate are gradually close to the substrate with increasing horizontal coordinate x, and exhibit a smaller potential gradient at the symmetry axis ($x = 0$ mm) and a larger potential gradient at the edge ($x = 60$ mm). Since the plasma must bypass the substrate to reach the other side of the substrate, the plasma density at the symmetry axis is lower than that at the edge, resulting in a weaker effect on raising the spatial potential. The potential distribution near the vacuum chamber wall in Fig. 5(b) reveals that the equipotential lines gradually move away from the vacuum chamber wall with increasing horizontal coordinate x, which reflects the transport process of the plasma along the vacuum chamber wall. Therefore, the results calculated by the PIC/MCC model with FEM solver for non-uniform grids clearly reflect the interactions between the spatial electromagnetic field and plasma in a vacuum system with a large size and complex geometric features.

With regard to the ion deposition process, conventional simulation techniques usually assume that the potential outside the plasma discharge region is constant.[23,24,28] In comparison, the spatial potential distribution obtained by the PIC/MCC model with FEM solver for non-uniform grids shows interactions between the electromagnetic field and plasma, which are, in fact, more consistent with physical reality.[26] To further compare the influence of the two types of potential distributions on the deposition process, the movements of the ions in the simulation domain under both potentials are calculated, and the ion deposition distributions on the substrate surface facing the target are shown in Fig. 6. Taking the steady-state ion matrix as the initial value, the test ion MC model (Appendix D) releases 10^5 ions originally. The calculation results show that the total number of ions deposited on the substrate increased from 8022 under the constant potential to 26132 under self-consistent potential, which means ion deposition proportion is 8.02% and 26.13% respectively. It is obvious that ion deposition is significantly enhanced because of the electric field, increasing the ion deposition proportion by more than 3 times compared with the constant potential. Besides, the average ion deposited energy under self-consistent potential is 49.7 eV, which is more than 45.0 eV larger than that at the constant potential (0.8 eV), indicating that the background electric field plays a significant role in attracting ions and increasing ion energy. The probability of the deposited ion density increases to some extent with the horizontal coordinate$x$ under the constant potential in Fig. 5(b), because the ions diffuse according to only the ion density gradient, leading to the ion deposition probability at the edge of the substrate ($x = 60$ mm) larger than at the symmetry axis ($x = 0$ mm). Under the background electric field shown in Fig. 4(d), the ion deposition probability is particularly high and relatively low in the range of 0 mm$< x <$20 mm and 20 mm$< x <$50 mm respectively, indicating the process of ion transport to the middle area of the substrate. However, with increasing horizontal coordinate x, the equipotential lines compress the space, in which the ions are subjected to strong electric fields, resulting in a larger deposition probability again at the edge of the substrate ($x = 60$ mm).

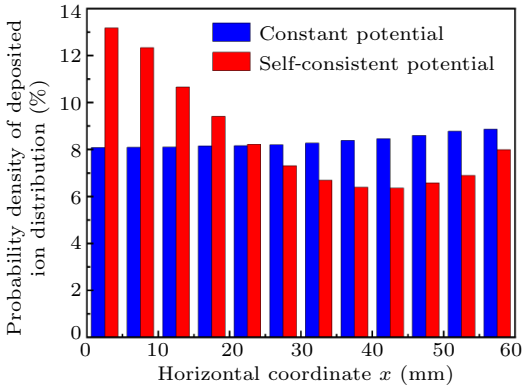


Fig. 6. Distribution of deposited ions on the substrate surface faced to the target.

Figure 7 illustrates the evolution of the potential distributions between the cathode and substrate versus discharge time. The sheath above the cathode becomes thinner, with the internal equipotential lines being compressed, resulting in a continuous increase in the potential gradient.[26] The potential almost stops changing at 0.3 μs, while the electrons and ions form stable accumulation in the discharge region (Figs. 4(a) and 4(b)). The criterion of steady state in the simulation is the convergence of electric potential.[29] Here, we select several fixed points in the simulation domain and track their temporal evolutions of the electric potential,[30] as shown in Fig. 8. The electric potentials stabilize with negligible fluctuations after 0.20 μs, indicating that the discharge had reached steady state,[25] and the calculations have converged. The fluid model and PIC/MCC method are also used to simulate a large and geometrically complex space independently, but no effective computational results are obtained. The former is unstable and fails to converge, while the latter needs over 1.4×10^7 grids (with a grid size of 1×10^{-4} m), resulting in the computation much larger than the server capacity. Hence, the program cannot be executed. In comparison, the PIC/MCC model with FEM solver for non-uniform grids yields stable simulation results in 0.3 μs with a grid of only 8.9×10^5 (only 6.3% of that required by the PIC/MCC method), showing a significant improvement in both the convergence and computation speed (Appendix E). Therefore, in large vacuum systems with complex geometric boundaries, the PIC/MCC model with FEM solver for non-uniform grids overcomes the limitations of the traditional fluid model and PIC/MCC method and demonstrates remarkable computation speed and convergence.

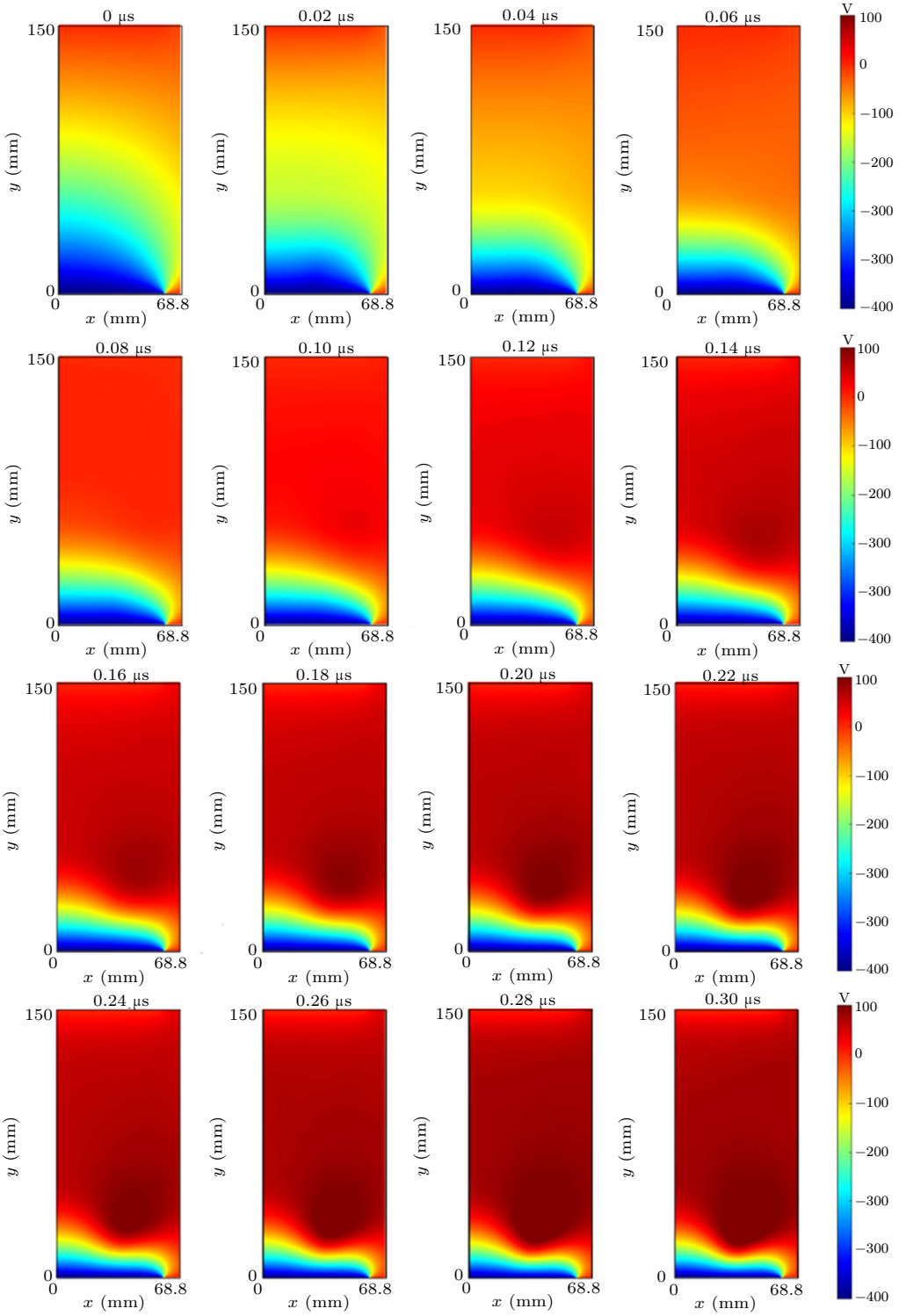


Fig. 7. Evolution of the potentials between the cathode and substrate in 0 μs–0.3 μs.

Figures 9(a) and 9(b) present the distributions of the electron density and electron temperature in the grid refinement area $\boldsymbol{Q}$ in the steady state, respectively. The discharge region, in which the plasma has a high density and high energy, is smaller compared with the strong background gradient area (gray area in Fig. 2(f)). In order to further enhance the computational speed, the plasma Debye length, λ_{De} (in unit m), is introduced to refine the computational grids. The Debye length,[26] as described in Eq. (4), characterizes the scale of the plasma electrostatic interactions, and reflects the combined effects of the plasma density and energy distribution. Generally, the grid size should be controlled to be smaller than the Debye length to ensure the computational accuracy[7]

$$\lambda_{\mathrm{De}} = \sqrt{\varepsilon_0 T_{\mathrm{e}} / e n_{\mathrm{e}}}, \tag{4}$$

where T_{e} (in unit eV) is the electron temperature, n_{e} (in unit m^{-3}) is the electron density, and $e = 1.6 \times 10^{-19}$ C denotes the elementary charge. According to Eq. (2), the distribu-

tion of the Debye length in area $\boldsymbol{Q}$ is calculated and shown in Fig. 9(c). The Debye lengths are primarily distributed between 1×10^{-3} m–1×10^{-2} m. Specifically, in the square area defined by 20 mm$\leq x \leq$60 mm and 20 mm$\leq y \leq$60 mm (light green area), the Debye length is small and shows a large variation gradient ranging from 1×10^{-3} m to $1\times10^{-2.5}$ m. Therefore, we retain the ultra-fine grid division only in this area, while in the other areas (yellow area), the grid size is set to 5×10^{-4} m, as shown in Fig. 8(d). The actual grid is shown in Fig. A2 of the Appendix A. Consequently, the grid quantity of the entire simulation domain is further reduced from 8.9×10^5 to 4.0×10^5 to improve the computational efficiency in one ion-step by 30%. Recalculation with the computational grids modified according to the Debye length shows the same magnitude and distribution of the plasma density as those calculated by the primary grids. The peak densities are 1.31×10^{15} m^{-3} and 1.30×10^{15} m^{-3} before and after the grid modification, respectively, showing a difference of less than 1%, as shown in Fig. 10. This indicates that the good stability of the PIC/MCC model with FEM solver for non-uniform grids is not influenced by the reduced grid quantity. However, the convergence process of the model is significantly accelerated from 0.3 μs to 0.26 μs, indicating that the simulation time is shortened. Due to the increased computational efficiency of single steps and reduced total steps, the total runtime to reach the steady state is shortened by approximately 40%, and the specific calculation process is shown in the Appendix.

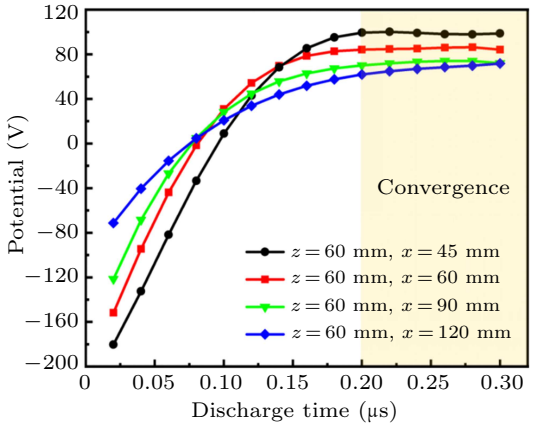


Fig. 8. The temporal evolution of the potential at different points.

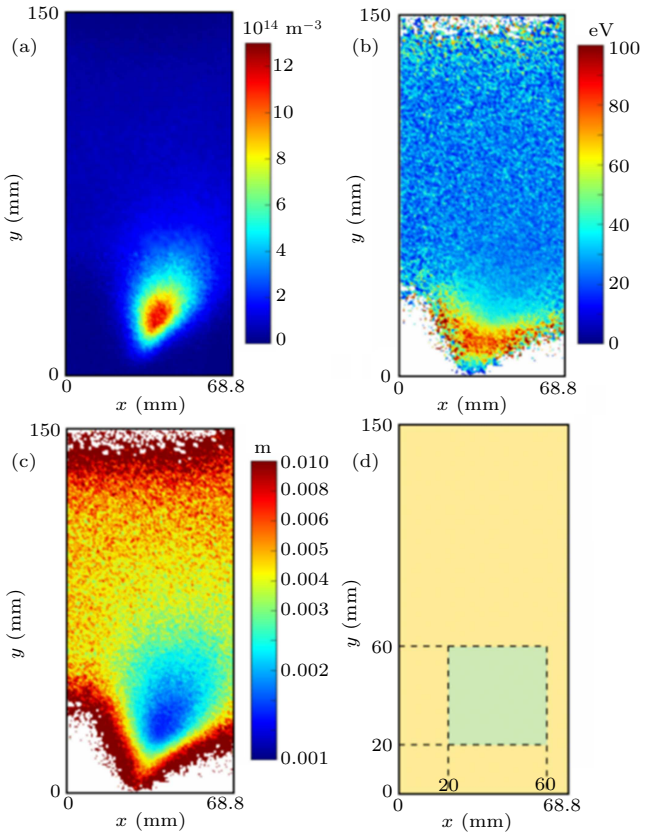


Fig. 9. Steady-state distributions: (a) electron density, (b) electron temperature, (c) the Debye length in the grid refinement area $\boldsymbol{Q}$, and (d) schematic diagram of the grid division according to the Debye length.

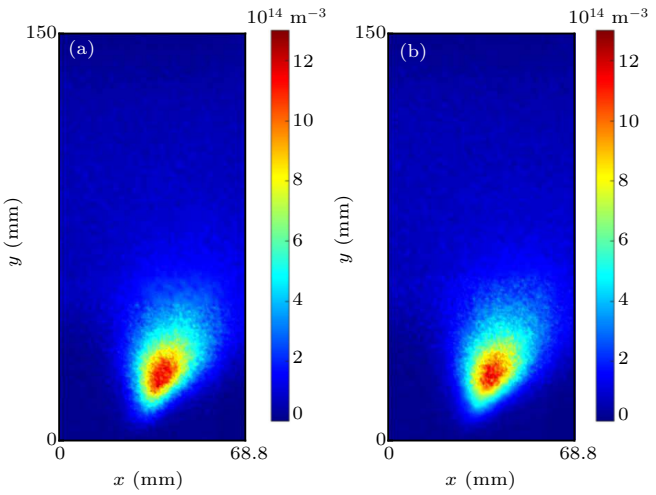


Fig. 10. Steady-state plasma distributions: (a) primary grids (0.3 μs) and (b) grids modified according to the Debye length (0.26 μs).

The PIC/MCC model with FEM solver for non-uniform grids proposed in this study enables plasma simulations in large-scale domains with complex geometries where process significant difference in plasma density at different locations. With this model, the influence on plasma discharge and transport of the discharge mountings (such as substrate, auxiliary anode, shielding plate, bias voltage, geometry, and so on) can be systematically characterized. And the results, including the plasma distribution, ion energy, etc. should be important reference to the layout of the whole coating systems. Furthermore, this model can be used in more complex vacuum systems, particularly for multi-target co-sputtering and multi-source coupling discharges, to describe the interactions between plasmas generated by different sources. Therefore, the coating performance can also be inferred by controlling magnetic field, position, and process of each plasma source.

4. Conclusion

To address the simulation challenges of plasma discharge in large-scale vacuum systems with complex geometric boundaries, a PIC/MCC model with FEM solver for non-

uniform grids is established by constructing a large simulation domain with complex boundaries by the fluid model and tracking the movements of charged particles in the inhomogeneous electromagnetic field by the PIC/MCC method. The calculations of the planar cathode discharge process in a large circular vacuum chamber reveal that the spatial electromagnetic field interacts with the plasma on the scale of the vacuum chamber. Consequently, the deposited ions exhibit a distribution consistent with the potential gradient of the sheath, thus increasing the ion deposition proportion and average ion energy by over 3 times and 45.0 eV respectively. The spatial potential reaches the steady state at 0.3 μs, accompanied by stable plasma accumulation in the discharge region. The model achieves convergence in 0.3 μs, presenting excellent operational speed and convergence. Based on the calculation grids modified by the Debye length, the model not only shows the same simulation results in the steady state, but also a convergence process compressed to 0.26 μs and the total running time reduced by 40%.

Appendix A: Actual grid division

The actual grids according to the discharge region is shown in Fig. A1. Specifically, in the strong background gradient area (0 mm $\leq x \leq$ 68.8 mm, 0 mm$\leq y \leq$60 mm), the grid size is 1×10^{-4} m. In the weak background gradient area (0 mm$\leq x \leq$68.8 mm, 60 mm$\leq y \leq$150 mm), the grid size is 5×10^{-4} m. In the other area, the grid size is 0.01 m. Additionally, the grid is divided according to the above parameters, and 100 steps are run from the generation of initial particles, with the running time of 56.6 hours.

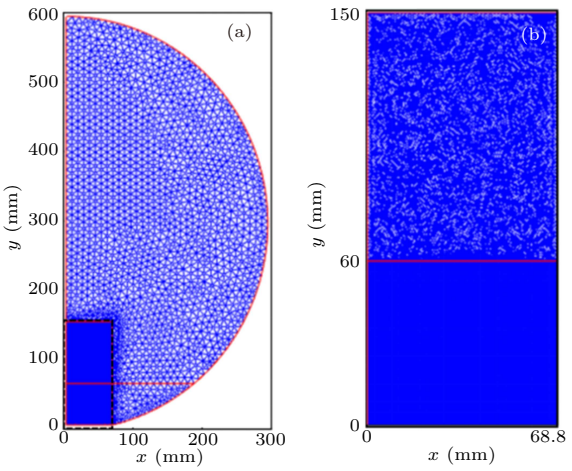


Fig. A1. Actual grids according to the discharge region.

The actual grids according to the Debye length is shown in Fig. A2. In the area with a smaller Debye length (20 mm$\leq x \leq$60 mm, 20 mm$\leq y \leq$ 60 mm), the grid size is 1×10^{-4} m. In the area with a larger Debye length (0 mm$\leq x \leq$60 mm, 0 mm$\leq y \leq$150 mm, except the subdivided square area), the grid size is 5×10^{-4} m. In the other area, the grid size is 0.01 m. And 100 steps are run from the generation of initial particles as well, which only takes 39.8 hours after adjusting grids, saving 16.8 hours compared with the former. So the computational efficiency of each step is greatly improved and the runtime is reduced by 30%. What is more, the convergence process is further shortened from 0.3 μs to 0.26 μs. Combining these two factors, the total runtime of dividing grids according to the Debye length is compressed by 40% approximately compared with dividing grids according to the discharge region, and the specific calculation process is described by

$$1-\frac{56.6-39.8}{56.6}\times100\%=70.3\%,$$
$$\frac{0.3-0.26\times70.3\%}{0.3}=39.1\%. \tag{A1}$$

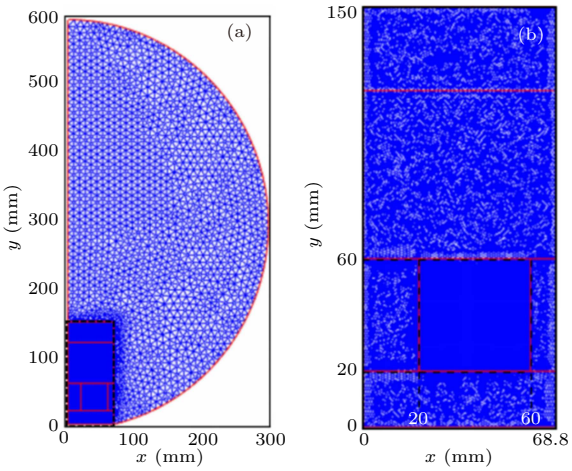


Fig. A2. Actual grids according to the Debye length.

Appendix B: Details of the PDETOOL

Various geometric shapes are constructed in PDETOOL, as shown in Fig. B1. The regions $\boldsymbol{Z}_1$, $\boldsymbol{Z}_2$, and $\boldsymbol{Z}_3$ represent the vacuum chamber, magnetron cathode, and substrate, respectively. The region Sym serves as a symmetric part to assist in simplifying the calculation. The shapes are combined and deducted through set operations, as described by the formula $(\boldsymbol{Z}_1-\boldsymbol{Z}_2-\boldsymbol{Z}_3)$-Sym, to form a complex simulation domain assembly.

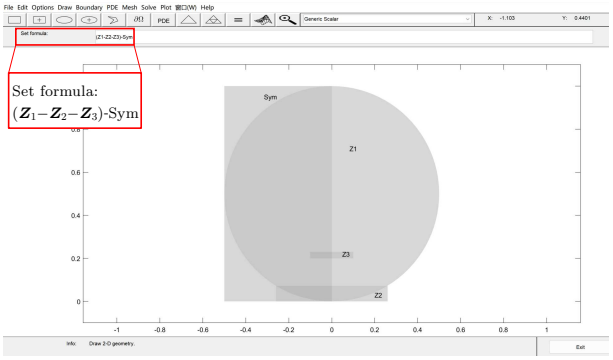


Fig. B1. Schematic diagram of geometry construction in PDETOOL.

According to the geometric structure of the simulation domain, the boundary conditions are set by the "applyBoundaryCondition" function of MATLAB. The specific equations

of Dirichlet and Neumann conditions are as shown as

$$h \times u = r, \tag{B1}$$

$$n \times c \times grad(u) + qu = g. \tag{B2}$$

Figure B2 shows the schematic diagram of boundary condition setting in PDETOOL. The fixed potential boundaries include the anode boundary, the cathode boundary, the transitional boundary, and the substrate boundary, which meet the Dirichlet condition, where $h = 1$, $r = C$ (constant value of the corresponding potential). The symmetrical boundary meets the Neumann condition, where $g = 0$, $q = 0$. The "generateMesh" function of MATLAB is used to divide the irregular grid with local refinement, and finally export the geometric structure, boundary conditions, grid nodes as matrix.

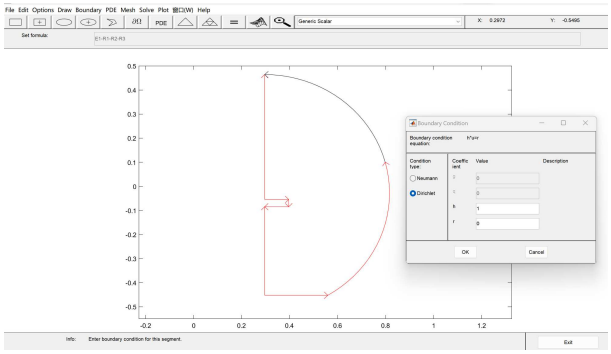


Fig. B2. Schematic diagram of boundary condition setting in PDETOOL.

The general form of solving partial differential equations in PDETOOL (Eq. (B3) is as follows:

$$m\frac{\partial^2 u}{\partial t^2} + d\frac{\partial u}{\partial t} - \nabla \cdot (c\nabla u) + au = f. \tag{B3}$$

According to the Poisson equation, the various parameters in Eq. (B2) are determined, that is, $m = 0$, $d = 0$, $c = e_0$ (unit charge number, 1.6×10^{-19} C), $a = 0$, and f represents the net charge density on the triangular grid nodes, which is obtained by interpolating and transforming the electron and ion density on the rectangular grid. The "specifyCoefficients" function of MATLAB is used to set the equation parameters. Finally, the partial differential equation is solved by "solvepde" function of MATLAB. The electric field strength in the x and y directions is solved by the gradient function of the potential (Eqs. (B4) and (B5))

$$E_x = \frac{\partial \varphi}{\partial x}, \tag{B4}$$

$$E_y = \frac{\partial \varphi}{\partial y}, \tag{B5}$$

where E_x (in unit V/m) and E_y (in unit V/m) are the electric field strength in the x and y directions, respectively, and x (in unit m) and y (in unit m) represent the horizontal and vertical coordinates of the particle.

Appendix C: Collision determination

Collisions of the particles are determined by the comparison between a random number $R_{\rm coll}$ ($0 < R_{\rm coll} < 1$) and collision probability $P_{\rm coll}$ could be expressed by

$$P_{\rm coll} = 1 - \exp(-N_0 \sigma v \Delta t), \tag{C1}$$

where N_0 (in unit m^{-3}) is the density of Ar atoms, σ (in unit m^2) is the collision cross section, and v (in unit m/s) is the particle velocity. The specific collision type is determined according to Table C1. Elastic collisions, ionization collisions, and excitation collisions may occur between electrons and Ar atoms, and the collision cross section is obtained by interpolation from the database based on the electron energy according to Table 1. Elastic collisions and charge exchange collisions may occur between Ar^+ ions and Ar atoms, which are regarded as hard-sphere collisions with σ determined only by the particle radius,

$$\sigma = \pi (R_{\rm i} + R_{\rm a})^2, \tag{C2}$$

where $R_{\rm i}$ (in unit m) and $R_{\rm a}$ (in unit m) represent the ion and atomic radius, respectively. For Ar, it is assumed that $R_{\rm i} = R_{\rm a} = 1.88 \times 10^{-10}$ m.[26]

Table C1. The decision condition of the specific collision types.

	Case	Collision type
Ar^+	$0 \le R_{\rm coll} \le P_{\rm el}$	elastic collision
	$P_{\rm el} < R_{\rm coll} \le P_{\rm el} + P_{\rm chex}$	charge exchange collision
	$P_{\rm el} + P_{\rm chex} < R_{\rm coll} \le 1$	no collision
e	$0 \le R_{\rm coll} \le P_{\rm el}$	elastic collision
	$P_{\rm el} < R_{\rm coll} \le P_{\rm el} + P_{\rm iz}$	ionization collision
	$P_{\rm el} + P_{\rm iz} < R_{\rm coll} \le P_{\rm el} + P_{\rm iz} + P_{\rm ex}$	excitation collision
	$P_{\rm el} + P_{\rm iz} + P_{\rm ex} < R_{\rm coll} \le 1$	no collision

Appendix D: Test ion MC model

At the initial, 10^5 Ar^+ ions are released from the region (0 mm$< x <$68.8 mm, 0 mm$< y <$60 mm) according to the steady-state ion density (Fig. 4(b)) calculated by the PIC/MCC model with FEM solver for non-uniform grids. The initial ion velocities follow the Maxwell distribution, with the average value equal to the Bohm velocity.[26] At the constant potential, the background electric field intensity is zero, and the test ion movement is governed exclusively by magnetic field effects and collision with background gas (Appendix C). While at the self-consistent potential, the background electric field intensity in the entire vacuum chamber is calculated according to the steady-state potential distribution (Fig. 4(d)). The test ions will rebound when they reach the symmetrical boundary, and disappear when they reach the target surface and the vacuum chamber wall. The test ions deposit at the substrate, and their positions and energies are recorded.

Appendix E: Comparison of computation speed

The standard PIC method requires 1.4×10^7 grids, resulting in an extremely large computing quantity even by the computing cluster. Therefore, we have to perform the quantitative comparison by running the first 1000 time-steps and recording the computational time with the standard PIC method and the PIC/MCC model with FEM solver for non-uniform grids, as shown in Fig. E1. The computation time of the PIC/MCC model with FEM solver for non-uniform grids was only 20740 s which is just 6.5% of the PIC model (314637 s), demonstrating a significant improvement in the computational performance. The main difference which causes the improved computational speed is that the PIC/MCC model with FEM solver for non-uniform grids can deal with non-uniform grids by the finite element method whereas the standard PIC method based on the finite difference method is only suitable to uniform grids.

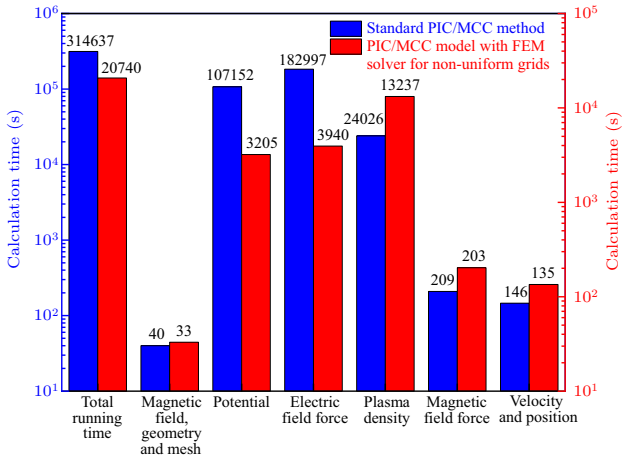


Fig. E1. The computational performance of the first 1000 time-steps with the standard PIC method and the PIC/MCC model with FEM solver for non-uniform grids.

Acknowledgements

Project supported by the Shenzhen Science and Technology Research Grants (Grant Nos. SGDX20201103095406024 and KJZD20231023100304009), the National Key Research and Development Program of China (Grant No. 2023YFA1608802), the Sustainable Supporting Funds for Colleges and Universities in 2022 (Grant No. 20220810143642004), the National Natural Science Foundation for Youth Science Fund Project (Grant No. 52305174), the Postdoctoral Research Fund after Outbound of Shenzhen (Grant No. 6700200201), Shenzhen–Hong Kong Technology Cooperation Funding Scheme (TCFS) (Grant No. GHP/149/20SZ or CityU 9440296), City University of Hong Kong Internal Fund for ITF Projects (Grant No. 9678148), City University of Hong Kong Donation Research Grants (Grant Nos. DON-RMG 9229021 and 9220061), and City University of Hong Kong Strategic Research Grant (SRG) (Grant No. 7005505).

References

[1] Cui S H, Wu Z Z, Xiao S, Zheng B C, Chen L, Li T J, Fu R K Y, Chu P K, Tian X B, Tan W C, Fang D N and Pan F 2020 *J. Appl. Phys.* **127** 023301
[2] Gudmundsson J T 2020 *Plasma Sources Sci. Technol.* **29** 113001
[3] Bogaerts A, Bultinck E, Kolev I, Schwaederle L, Aeken K V, Buyle G and Depla D 2009 *J. Phys. D: Appl. Phys.* **42** 194018
[4] Lieberman M A 1989 *J. Appl. Phys.* **66** 2926
[5] Emmert G A and Henry M A 1992 *J. Appl. Phys.* **71** 113
[6] Xia Z Y and Chan C 1993 *J. Appl. Phys.* **73** 3651
[7] Birdsall C K 1991 *IEEE Trans. Plasma Sci.* **19** 65
[8] Kolev I and Bogaerts A 2009 *J. Vac. Sci. Technol. A* **27** 20
[9] Bultinck E and Bogaerts R 2009 *New J. Phys.* **11** 103010
[10] Wu C S and Gao C Y 2019 *Methods of Mathematical Physics* (3rd edn.) (Beijing: Peking University Press) p. 174
[11] Costin C, Marques L, Popa G and Gousset G 2005 *Plasma Sources Sci. Technol.* **14** 168
[12] Kolev I and Bogaerts A 2004 *Contrib. Plasma Phys.* **44** 582
[13] Jimenez F J and Dew S K 2012 *J. Vac. Sci. Technol. A.* **30** 041302
[14] Jimenez F J, Dew S K and Field D J 2014 *J. Vac. Sci. Technol. A.* **32** 061301
[15] Sobbia R, Browning P K and Bradley J W 2008 *J. Vac. Sci. Technol. A.* **26** 103
[16] Nanbu K 2000 *IEEE Trans. Plasma Sci.* **28** 971
[17] Wang H Y, Jiang W and Wang Y N 2010 *Plasma Sources Sci. Technol.* **19** 045023
[18] Vay J L, Colella P, Mccorquodale P, Straalen B V, Friedman A and Grote D P 2002 *Laser Part. Beams.* **20** 569
[19] Vay J L, Colella P, Kwan J W, Mccorquodale P, Serafini D B, Friedman A, Grote D P, Westenskow G, Adam J C and Héron A 2004 *Phys. Plasmas.* **11** 2928
[20] Cui S H, Guo Y X, Chen Q H and Wu Z Z 2022 *China Surf. Eng.* **35** 23
[21] Banegas A 1978 *Math. Comput.* **32** 441
[22] Wang H Y, Jiang W and Wang Y N 2009 *Comput. Phys. Commun.* **180** 1305
[23] Cui S H, Wu Z Z, Lin H, Xiao S, Zheng B C, Liu L L, An X K, Fu R K Y, Tian X B, Tan W C and Chu P K 2019 *J. Appl. Phys.* **125** 063302
[24] Cui S H, Guo Y X, Chen Q H, Jin Z, Yang C, Wu Z C, Su X Y, Ma Z Y, Tian X B and Wu Z Z 2022 *Acta Phys. Sin.* **71** 055203 (in Chinese)
[25] Bultinck E, Kolev I, Bogaerts A and Depla D 2008 *J. Appl. Phys.* **103** 013309
[26] Lieberman M A and Lichtenberg A J 2005 *Principles of Plasma Discharges and Materials Processing* (New York: Wiley)
[27] Raadu M A and Axnäs I 2011 *Plasma Sources Sci. Technol.* **20** 065007
[28] Cui S H, Wu Z Z, Xiao S, Chen L, Li T J, Liu L L, Fu R K Y, Tian X B, Chu P K and Tan. W C 2019 *Acta Phys. Sin.* **68** 195204 (in Chinese)
[29] Straaten T A V D, Cramer N F, Falconer I S, *et al.* 1999 *J. Phys. D: Appl. Phys.* **31** 177
[30] Cui S H, Chen Q H, Guo Y X, *et al.* 2022 *J. Phys. D: Appl. Phys.* **55** 325203